UC Berkeley
SEMM Reports Series

Title
An Analysis of Strong Discontinuities in a Saturated Poro-Plastic Solid

Permalink
https://escholarship.org/uc/item/051792s5

Authors
Armero, Francisco
Callari, Carlo

Publication Date
1998-10-01

eScholarship.org Powered by the California Digital Library
University of California

REPORT NO.
UCB/SEMM-98/11

STRUCTURAL ENGINEERING
MECHANICS AND MATERIALS

AN ANALYSIS OF STRONG DISCONTINUITIES IN A SATURATED PORO-PLASTIC SOLID

BY

F. ARMERO

AND

C. CALLARI

OCTOBER 1998

DEPARTMENT OF CIVIL AND ENVIRONMENTAL ENGINEERING
UNIVERSITY OF CALIFORNIA, BERKELEY

An Analysis of Strong Discontinuities in a Saturated Poro-Plastic Solid

by

F. ARMERO & C. CALLARI*

Structural Engineering, Mechanics and Materials
Department of Civil and Environmental Engineering
University of California, Berkeley CA 94720, USA

Abstract

We present in this paper an analysis of strong discontinuities in fully saturated porous media in the infinitesimal range. In particular, we describe the incorporation of the local effects of surfaces of discontinuity in the displacement field, and thus the singular distributions of the associated strains, from a local constitutive level to the large scale problem characterizing the quasi-static equilibrium of the solid. The characterization of the flow of the fluid through the porous space is accomplished in this context by means of a localized (singular) distribution of the fluid content, that is, involving a regular fluid mass distribution per unit volume and a fluid mass per unit area of the discontinuity surfaces in the small scale of the material. This framework is shown to be consistent with a local continuum model of coupled poro-plasticity, with the localized fluid content arising from the dilatancy associated with the strong discontinuities. More generally, complete stress-displacement-fluid content relations are obtained along the discontinuities, thus identifying the localized dissipative mechanisms characteristic of localized failures of porous materials. The proposed framework also involves the coupled equation of conservation of fluid mass and seepage through the porous solid via Darcy's law, and considers a continuous pressure field with discontinuous gradients, thus leading to discontinuous fluid flow vectors across the strong discontinuities. All these developments are then examined in detail for the model problem of a saturated shear layer of a dilatant material. In particular, enhanced finite element methods are developed in this framework for this particular problem. The finite elements accommodate the different localized fields described above at the element level. Several representative numerical simulations are presented illustrating the performance of the proposed numerical methods.

Key Words: Porous media, elastoplasticity, strain localization, strong discontinuity, enhanced finite element methods, coupled problems.

---

* Currently at Dipartimento di Ingegneria Civile Università degli Studi di Roma "Tor Vergata" Via di Tor Vergata, 00133 Roma, Italy

1. Introduction

The study of localized failures of solids is of the main interest given its important practical applications. In the case of porous materials, like typical geomaterials, the coupling of the flow of a fluid through the porous space is known to have significant effects in this type of failures. In this way, the localization of the strains in narrow bands, referred to as shear bands given their nature, results also in the concentration of the fluid flow along them, leading altogether to the final collapse of the solid. Theoretical and numerical analyses of these phenomena abound in the literature; representative examples are given by RUDNICKI & RICE [1975], RICE [1975], LORET & PREVOST [1991], PIETRUSZCZAK [1995], SCHREFLER et al [1995], VARDOULAKIS [1996], and RUNESSON et al [1996], among many others.

The phenomenon of strain localization is common to many other materials including, for example, metals. In all the cases, the final stages of the deformation before failure are characterized by the localization of the dissipative effects along these band-type structures. Different approaches can be found in the literature to model and simulate numerically this phenomenon; a complete review falls outside the scope of this work. Of interest to the developments presented in this paper is the so-called strong discontinuity approach. This approach can be found developed for the purely mechanical problem in SIMO et al [1993], ARMERO & GARIKIPATI [1996] and OLIVER [1996], with the consideration of regularized strong-discontinuities in LARSSON & RUNESSON [1996] and STEINMANN et al [1997], among others. The resulting formulations consider the limit case of solutions involving a discontinuous displacement field, as they are necessarily obtained in (uncoupled) rate-independent plasticity models of the local continuum. The key feature, however, is the addition of *a localized dissipative mechanism* along these discontinuities, a feature not present in the original local continuum model. The resulting problem of evolution avoids the ill-posedness of the classical continuum problem (that is, it leads to unique solutions depending continuously on the data), as it has been shown in the closed-form analytical solutions presented in ARMERO [1997b] for the problem of wave propagation in a localized softening bar. Similarly, these ideas have been shown in ARMERO [1997a] to furnish a very general tool for the efficient modeling in the large scale of the localized effects of regularized models exhibiting a finite length scale (rate-dependent models, to be specific), while treating these small scales as unresolvable.

We present in this paper the extension of these ideas to the coupled case of a saturated poro-plastic solid. The goals are two-fold. The first objective is the characterization of strong discontinuities in this type of models. In particular, we consider poro-elastoplastic models in the infinitesimal range characterized by an additive decomposition of the strains and the fluid content (fluid mass per unit volume), that is, in the framework first proposed in the pioneering work of BIOT [1941] in the visco-elastic range. Complete details of these models can be found in the recent account in COUSSY [1995], including also several analyses of the resulting boundary value problems. In this context, discontinuous solutions in the

displacements, with the corresponding strains being a singular distribution, are shown to be consistent with the consideration of a localized fluid content (that is, with a fluid mass distributed per unit area of a dilatant surface), as a consequence of a discontinuity of the fluid flow in a permeable porous solid. Importantly, the pore pressure field remains continuous (or, more precisely, with regular gradients). This situation is to be contrasted with the analyses presented in RUNESSON et al [1996] and LARSSON et al [1996] for the limit undrained case, where a discontinuity of the pressure field was considered. For the case of a finite permeability in Darcy's law, this assumption would require to evaluate second derivatives of a discontinuous field. This mathematical structure of the equations for a positive permeability, as well as experimental evidence (see e.g. VARDOULAKIS [1996]), seem then to indicate as more appropriate the continuity assumption on the pressure field. We develop then in this context an analysis of the considered strong-discontinuities in the displacement field for classical continuum models with strain softening (following closely the work of SIMO et al [1993]), as a motivation for the form of the localized stress-displacement-fluid content relations characterizing the localized dissipative mechanisms in these solutions.

An understanding of these analyses is gained by the consideration of a saturated shear layer of a dilatant porous solid; see e.g. RICE [1975] for a linearized stability analysis of this case. We derive complete localized laws for this model problem based on the Mohr-Coulomb associated plastic potential. In particular, the dilatancy associated with the discontinuity for this model is identified as the origin of the localized fluid content. In the context considered herein, and in agreement with RUDNICKI & RICE [1975] and this last reference, among many others, the inception of localization is observed to be determined by the drained response of the material. The case of a strain softening drained response leads to a lack of a length scale associated with the strain localization in the shear component of the deformation, as indicated in RICE [1975] or, in a more general context, in ZHANG & AL [1998].

All these relations lead directly to the formulation of enhanced strain finite element methods for the solution of this particular model problem, the second goal of this paper. The methodology proposed in ARMERO & GARIKIPATI [1995,96], without introducing a regularization of the singular strain field, is considered. We present complete details for the geometrically one-dimensional problem of the dilatant shear layer; extensions to more general situations are currently under further investigation. The proposed enhanced finite elements involve a constant approximation at the element level of the displacement jumps appearing in the expressions of the singular strains and of the localized fluid content. The new methods lead to a correct resolution of the energy dissipation associated to the localized solutions, thus avoiding the pathological mesh-dependence observed in standard isoparametric formulations of continuum softening models in this shear driven problem.

An outline of the rest of the paper is as follows. Section 2 includes a complete characterization of strong discontinuities in porous media. More specifically, the large-

scale problem defining the equilibrium of the solid is summarized in Section 2.1, with the introduction of the strong discontinuities in the small scale done in Section 2.2. The consequences of these considerations in the flow of a fluid through the porous solid are studied in Section 2.3. Section 3.2 derives the localized stress-displacement-fluid content laws motivated by a general continuum model presented in Section 3.1. The applications of these developments to the model problem of the dilatant shear layer is undertaken in Section 4, including the development of the enhanced finite element formulation for this case in Section 4.2. After the discussion of several numerical simulations in Section 5, we present in Section 6 several concluding remarks as well as a discussion of additional aspects of the problem currently under investigation.

2. A Characterization of Discontinuous Solutions in Porous Media

We describe in this section the general equations of the coupled problem of evolution for the saturated porous solid of interest in this work. The presentation follows the ideas originally proposed in ARMERO [1997a] for the uncoupled mechanical problem, characterizing the localized effects in the deformation processes of solids through the consideration of strong discontinuities *locally* in the small scales. In this context, Section 2.1 describes the mechanical governing equations of the classical local continuum problem, the *large-scale problem* as referred to in this work, involving regular displacement fields. The kinematics of strong discontinuities is described next in Section 2.2. The addition of the fluid flow fields in this context is developed in Section 2.3.

2.1. The large-scale mechanical problem

We consider a porous solid, composed of a solid skeleton and (non-occluded) porous space, occupying the reference placement $\Omega \subset \mathbb{R}^{n_{\text{dim}}}$ ($n_{\text{dim}} = 1, 2$ or 3) identified with its current placement under the usual assumption of infinitesimal strains. In this context, the deformation of the solid in the large scale can be characterized by the displacement $\boldsymbol{u} : \Omega \times [0, T] \to \mathbb{R}^{n_{\text{dim}}}$ of the solid's skeleton for a typical time interval T. Essential boundary conditions $\boldsymbol{u} = \bar{\boldsymbol{u}}$ are imposed on $\partial_u \Omega \subset \partial\Omega$, the boundary of the domain Ω; see Figure 2.1. The space of admissible displacement variations, satisfying the homogeneous counterpart of these essential boundary conditions,

$$\mathcal{V}_u = \{\boldsymbol{\eta} : \Omega \to \mathbb{R}^{n_{\text{dim}}} \quad : \quad \boldsymbol{\eta} = 0 \quad \text{on} \quad \partial_u \Omega\} \ , \tag{2.1}$$

is considered as usual.

The large-scale property attached to the displacement field $\boldsymbol{u}$ and corresponding variations in $\mathcal{V}_u$ refers to the fact that standard regularity conditions are assumed for

these fields. By standard, we refer to functions having integrable absolute derivatives (that is, the derivatives being regular distributions as opposed to singular distributions, in the usual sense; see e.g. STAKGOLD [1979]) at the least. Additional localized effects, in the form of discontinuous displacement fields with strains being singular distributions, are considered separately in Section 2.2 below. In this context, the infinitesimal *large-scale strain* field is given by the standard relation

$$\boldsymbol{\varepsilon} = \nabla^s \boldsymbol{u} = \tfrac{1}{2} \left[\nabla \boldsymbol{u} + (\nabla \boldsymbol{u})^T \right] , \tag{2.2}$$

for the symmetric part of the gradient operator $\nabla(\cdot)$, with $(\cdot)^T$ denoting the transpose of a tensor.

Denoting the (total) stress field in the solid by $\boldsymbol{\sigma} \in \mathbb{R}^{n_{\text{dim}} \times n_{\text{dim}}}$ (symmetric), the quasi-static equilibrium of the solid is then be expressed by the classical relation

$$\int_\Omega \boldsymbol{\sigma} : \nabla^s \boldsymbol{\eta} \, d\Omega = \int_\Omega \boldsymbol{f} \cdot \boldsymbol{\eta} \, d\Omega + \int_{\partial_t \Omega} \bar{\boldsymbol{t}} \cdot \boldsymbol{\eta} \, dA , \qquad \forall \boldsymbol{\eta} \in \mathcal{V}_u , \tag{2.3}$$

for the volume $d\Omega$ and area dA elements (i.e., the Lebesgue measures in $\Omega \subset \mathbb{R}^{n_{\text{dim}}}$ and $\partial\Omega \subset \mathbb{R}^{n_{\text{dim}}-1}$, respectively), volumetric body force $\boldsymbol{f}$, and imposed tractions $\bar{\boldsymbol{t}}$ on $\partial_t \Omega \subset \partial\Omega$. The assumptions

$$\partial_u \Omega \cap \partial_t \Omega = \emptyset \quad \text{and} \quad \overline{\partial_u \Omega \cup \partial_t \Omega} = \partial\Omega , \tag{2.4}$$

are considered as usual. The equation (2.3) corresponds to the classical form of the principle of virtual work and leads, after a standard argument, to the local equilibrium equations. In particular, we also have the continuity relation across any material surface Γ with unit normal $\boldsymbol{n}$

$$[\![\boldsymbol{\sigma}]\!] \boldsymbol{n} = \boldsymbol{0} , \tag{2.5}$$

for the jump in the stress $[\![\boldsymbol{\sigma}]\!]$ across Γ. The classical notion of the traction vector on Γ

$$\boldsymbol{t}_\Gamma := \boldsymbol{\sigma} \boldsymbol{n} \Big|_\Gamma \tag{2.6}$$

is then recovered.

2.2. The kinematics of strong discontinuities

The large-scale problem defined in the previous section accounts for solutions involving standard regularity conditions of the different fields, as indicated above. However, it is of the main interest to characterize more general solutions and, in particular, discontinuities in the displacement field, the so-called *strong discontinuities,* leading to strains being singular distributions. The purpose of this generalization is to model efficiently

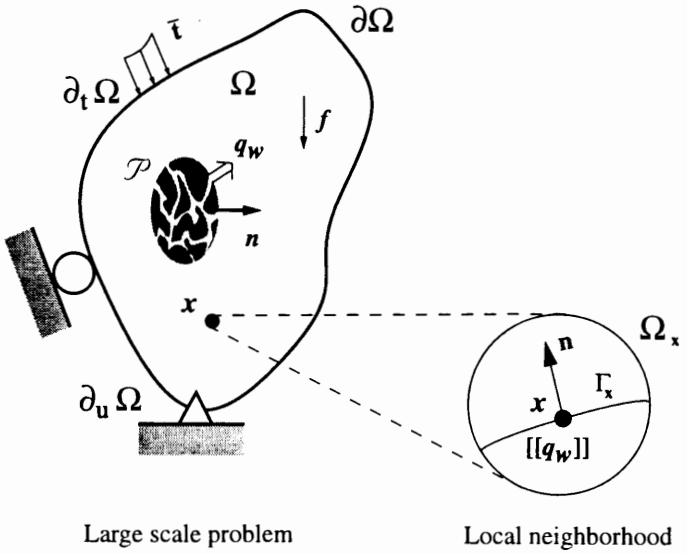

FIGURE 2.1. Kinematics of strong discontinuities. Large-scale problem defining the equilibrium of the solid, with standard loading and boundary conditions, and the local neighborhood Ω_x incorporating the effects of the strong discontinuities. The flow of fluid in the porous solid is characterized by the flow vector $\boldsymbol{q}_w$, which exhibits a discontinuity across Γ_x.

(both theoretically and numerically) the localized response of inelastic solids as discussed in Section 3 below. Following ARMERO [1997a], these localized (non-smooth) effects are introduced at the local level as follows.

Let $\Omega_x \subset \Omega$ be a local neighborhood of a material point $\boldsymbol{x} \in \Omega$. The case of interest corresponds to the appearance of a discontinuity in the displacement field across a certain orientation $\boldsymbol{n}$ at $\boldsymbol{x} \in \Omega_x$. Let Γ_x denote a surface in Ω_x with such orientation; see Figure 2.1 for an illustration of these ideas. As indicated below, the case of $measure(\Omega_x) \to 0$ is of the interest herein, thus allowing for this general local definitions. In this context, we consider a general function $\Psi_{\Gamma_x} : \Omega_x \to \mathbb{R}$ exhibiting a unit jump across the surface Γ_x, that is, $[\![\Psi_{\Gamma_x}]\!] = 1$ on Γ_x. Denoting by H_{Γ_x} the Heaviside step function across Γ_x the function Ψ_{Γ_x} can be expressed as

$$\Psi_{\Gamma_x} = H_{\Gamma_x} - N_{\Gamma_x} \qquad \text{in} \quad \Omega_x \,, \tag{2.7}$$

for a smooth function N_{Γ_x}.

With this notation, we consider the small-scale displacement field

$$\boldsymbol{u}_\mu = \boldsymbol{u} + \boldsymbol{\xi}\, \Psi_{\Gamma_x} \qquad \text{in } \Omega_x \,, \tag{2.8}$$

in terms of the large-scale displacement $\boldsymbol{u}$ and the local field $\boldsymbol{\xi} : \Omega_x \to \mathbb{R}^{n_{\text{dim}}}$ defining the displacement jump $[\![\boldsymbol{u}_\mu]\!] = \boldsymbol{\xi}$ across Γ_x. The infinitesimal strains corresponding to the

local displacement field $\boldsymbol{u}_\mu$, which we refer to as the *small-scale strains,* are given by

$$\boldsymbol{\varepsilon}(\boldsymbol{u}_\mu) = \underbrace{\boldsymbol{\varepsilon}(\boldsymbol{u}) + \boldsymbol{G}(\boldsymbol{\xi})}_{=:\ \bar{\boldsymbol{\varepsilon}}} + \underbrace{(\boldsymbol{\xi} \otimes \boldsymbol{n})\ \delta_{\Gamma_x}}_{} \ , \tag{2.9}$$

$\bar{\boldsymbol{\varepsilon}}$: *regular distribution*; $(\boldsymbol{\xi} \otimes \boldsymbol{n})\ \delta_{\Gamma_x}$: *singular distribution*

for the regular function

$$\boldsymbol{G}(\boldsymbol{\xi}) := \nabla^s \boldsymbol{\xi}\ H_{\Gamma_x} - \boldsymbol{\xi} \otimes \nabla^s N_{\Gamma_x} \ , \tag{2.10}$$

and the Dirac delta function δ_{Γ_x} across Γ_x. We note the result $\nabla H_{\Gamma_x} = \boldsymbol{n}\ \delta_{\Gamma_x}$ for the unit normal $\boldsymbol{n}$; see STAKGOLD [1979]. The relation (2.9) identifies the decomposition of the small-scale strain $\boldsymbol{\varepsilon}(\boldsymbol{u}_\mu)$ in regular and singular parts, the latter corresponding to the localized effects along the strong discontinuity Γ_x. Similarly, the decomposition (2.9) can be understood as defining the *unresolved strain* $\boldsymbol{\varepsilon}_{unres} = \boldsymbol{\varepsilon}(\boldsymbol{u}_\mu) - \boldsymbol{\varepsilon}(\boldsymbol{u})$ by the large-scale strain $\boldsymbol{\varepsilon}(\boldsymbol{u})$.

The considerations above have introduced the new unknown field $\boldsymbol{\xi}$, in addition to the large-scale displacements $\boldsymbol{u}$. As shown in ARMERO [1997a], a well-posed local continuum formulation can be constructed by considering the local weak equation for all variations $\boldsymbol{\gamma}$ of the local jumps $\boldsymbol{\xi}$

$$-\frac{1}{measure(\Omega_x)} \int_{\Omega_x} \boldsymbol{\gamma} \cdot \boldsymbol{\sigma}\boldsymbol{n}\ d\Omega + \frac{1}{measure(\Gamma_x)} \int_{\Gamma_x} \boldsymbol{\gamma} \cdot \boldsymbol{t}_{\Gamma_x}\ dA = 0 \ , \tag{2.11}$$

in the limit $h_x := measure(\Omega_x)/measure(\Gamma_x) \to 0$, imposing then the equilibrium equation (2.11). The whole formulation is to be understood in this local limit, thus avoiding the precise definition of the neighborhood Ω_x. The resulting large-scale local problem incorporates effectively the dissipative effects of the discontinuous solutions, and leads to a well-posed problem. See ARMERO [1997b] for the closed-form analysis of the wave propagation in a one-dimensional bar considering the resulting dynamic problem, showing the uniqueness of the solution and its continuous dependence on the data.

2.3. The characterization of the fluid flow

The porous solid is assumed to be fully saturated with a fluid. Following BIOT [1941], we consider the *fluid content* $\bar{M} : \Omega \times [0,T] \to \mathbb{R}$ increment (units of fluid mass per unit volume) over an initial value $M_o : \Omega \to \mathbb{R}$. Given the developments above for the discontinuous solutions in the displacements $\boldsymbol{u}_\mu$, and the corresponding singular strains $\boldsymbol{\varepsilon}(\boldsymbol{u}_\mu)$, we consider similarly the *localized fluid content* $\tilde{M}$ increment (units of fluid mass per unit area) on the set

$$\Gamma = \cup \Gamma_x = \{x \in \Omega \quad : \quad \Gamma_x \neq \emptyset\} \ , \tag{2.12}$$

composed by all the material points exhibiting locally strong discontinuities. We assume that this set defines a measure space (being, in general, of lower dimension than Ω, e.g., a surface), thus allowing the decomposition

$$M := \bar{M} + \tilde{M}\ \delta_\Gamma\ , \tag{2.13}$$

for the total fluid content M. In equation (2.13), we have introduced the notation δ_Γ for the delta function satisfying the integral relation

$$\begin{matrix}\text{Total fluid mass}\\ \text{in } \Omega\end{matrix} := \int_\Omega M\ d\Omega = \int_\Omega \bar{M}\ d\Omega + \int_\Gamma \tilde{M}\ dA\ , \tag{2.14}$$

for the corresponding measure dA on Γ and the usual Lebesgue measure $d\Omega$ in $\mathbb{R}^{n_{\text{dim}}}$. Physically, this relation identifies the fluid mass stored along all the strong discontinuities of the displacement. As discussed in Section 3 below, the decomposition (2.13) is consistent with continuum local models of poro-plasticity, with the localized fluid content $\tilde{M}$ given by the dilatancy associated to the strong discontinuities Γ.

Assuming that no fluid sources exist, the conservation of fluid mass in any part $\mathcal{P} \subset \Omega$ is given by

$$\int_\mathcal{P} \dot{M}\ d\Omega = -\int_{\partial\mathcal{P}} \boldsymbol{q}_w \cdot \boldsymbol{n}\ dA\ , \tag{2.15}$$

defining a vector field $\boldsymbol{q}_w$ that characterizes the local flow of fluid mass due to fluid conduction through the porous space of the solid. These ideas are illustrated in Figure 2.1. In (2.15), the time derivative has been denoted by $\dot{(\cdot)}$. A standard argument based on integration by parts leads to the relations

$$\dot{\bar{M}} = -\operatorname{div} \boldsymbol{q}_w \qquad \text{in } \Omega\backslash\Gamma\ , \tag{2.16}$$

and the localized balance law

$$\dot{\tilde{M}} = -[\![\boldsymbol{q}_w]\!] \cdot \boldsymbol{n} \qquad \text{on} \quad \Gamma\ , \tag{2.17}$$

for the unit normal $\boldsymbol{n}$ to Γ (the smoothness of Γ is assumed, for simplicity), identifying the discontinuity of the fluid flow with the jump term $[\![\boldsymbol{q}_w]\!]$ on Γ. We observe that the relations (2.16) and (2.17) can be written equivalently in distributional form as

$$\dot{M} = -\operatorname{div} \boldsymbol{q}_w \quad \left(= -\operatorname{div}\left[\boldsymbol{q}_w|_{\Omega\backslash\Gamma}\right] - [\![\boldsymbol{q}_w]\!] \cdot \boldsymbol{n}\ \delta_{\Gamma_x}\right)\ ; \tag{2.18}$$

see e.g. STAKGOLD [1979].

The classical local relation given by Darcy's law is assumed in the following developments for the fluid flow vector $\boldsymbol{q}_w$ in $\Omega\backslash\Gamma$, that is,

$$\boldsymbol{q}_w = -\rho_w^2 \boldsymbol{k}(\nabla\mu_w - \boldsymbol{g})\ , \tag{2.19}$$

in terms of the the density of the fluid ρ_w, the permeability tensor of the porous solid $\boldsymbol{k}$, gravity $\boldsymbol{g}$, and the free enthalpy (or chemical potential) μ_w of the fluid. We consider the case of a barotropic fluid characterized by its *pore pressure* $p : \Omega \times [0,T] \to \mathbb{R}$ and the constitutive relation

$$\widehat{\mu}_w(p) = \int^p \frac{d\eta}{\widehat{\rho}_w(\eta)} \,, \tag{2.20}$$

in the developments that follow. In this case, Darcy's law (2.19) takes the classical form

$$\boldsymbol{q}_w = -\rho_w \boldsymbol{k}(\nabla p - \rho_w \, \boldsymbol{g}) \,, \tag{2.21}$$

for the fluid mass flow vector $\boldsymbol{q}_w$ in $\Omega \backslash \Gamma$. The discontinuous part of the fluid flow $[\![\boldsymbol{q}_w]\!]$ on Γ is given by the localized fluid content $\tilde{M}$ through (2.17) and is obtained by the localized constitutive relations derived in the following section for a general elastoplastic porous solid. We note that the locality of all the previous arguments, that is, arising at a material point $\boldsymbol{x} \in \Omega$, leads to the pointwise relation (2.17), not accounting explicitly for flow conduction along the discontinuity surface Γ.

Finally, the weak form of the governing equations (2.16) and (2.17), as employed in the finite element methods developed in Section 4.2, are obtained multiplying equation (2.16) by a smooth test function $w : \Omega \to \mathbb{R}$, and integrating by parts, thus leading to

$$\int_\Omega \dot{\tilde{M}} \; w \; d\Omega = \int_\Omega \boldsymbol{q}_w \cdot \nabla w \; d\Omega - \int_{\partial\Omega} \boldsymbol{q}_w \cdot \boldsymbol{n} \; w \; dA + \int_\Gamma [\![\boldsymbol{q}_w]\!] \cdot \boldsymbol{n} \; w \; dA \,. \tag{2.22}$$

Assuming that the normal flow of fluid mass $\bar{q}_{wn}$ is known on the part of the boundary $\partial_p\Omega$ (possibly as a function of the pore pressure p), that is,

$$\boldsymbol{q}_w \cdot \boldsymbol{n} = \bar{q}_{wn} \qquad \text{on} \quad \partial_q\Omega \subset \partial\Omega \,, \tag{2.23}$$

with the part of the boundary with an imposed pressure denoted by $\partial_p\Omega$, equation (2.22) reduces to

$$\int_\Omega \dot{\tilde{M}} \; w \; d\Omega + \int_\Gamma \dot{\tilde{M}} \; w \; dA = \int_\Omega \boldsymbol{q}_w \cdot \nabla w \; d\Omega - \int_{\partial_q\Omega} \bar{q}_{wn} \; w \; dA \qquad \forall w \in \mathcal{V}_p \,, \tag{2.24}$$

after making use of the local relation (2.17). The notation

$$\mathcal{V}_p = \{ w : \Omega \to \mathbb{R} \;\; : \;\; w = 0 \;\; \text{on} \;\; \partial_p\Omega \} \,, \tag{2.25}$$

for the space of admissible pressure variations has been employed in (2.24). The assumptions (2.4) are similarly imposed for the parts of the boundary $\partial_p\Omega$ and $\partial_q\Omega$.

Remark 2.1. We emphasize the important fact that the pressure field p and the chemical potential $\mu_w = \hat{\mu}_w(p)$, as well as their variations, remain continuous (or, to be more precise,

with integrable absolute value derivatives) in all the previous developments, a situation to be contrasted with the formulations presented in e.g. LARSSON et al [1996] for the undrained limit, considering discontinuous pressure fields with the corresponding gradients being singular distributions. Mathematically, the structure of the local equation (2.18) with the flow vector given by (2.21), involving then the second spatial derivatives of the pressure field for a positive permeability, precludes these discontinuities, but not of the fluid flow vector. In addition, the presence of pressure shocks has not been observed experimentally; see e.g. VARDOULAKIS [1996]. In the proposed context, the flow jump $[\![\boldsymbol{q}_w]\!]$ can be related to a discontinuity in the pressure gradient instead. The discussion presented next identifies the consistency of this approach with a continuum poro-elastoplastic model. □

3. Localized Dissipative Mechanisms in Coupled Poro-Elastoplastic Solids

The governing equations described in the previous section characterize the kinematics as well as the quasi-static equilibrium and the conservation of fluid mass in a general porous media exhibiting strong discontinuities. In this context, the kinematic variables, consisting of the large-scale displacements $\boldsymbol{u}$ and the local displacement jumps $\boldsymbol{\xi}$, and the fluid variables, given by the (continuous) pore pressure p and the fluid content M (with its regular $\bar{M}$ and singular parts $\tilde{M}$), have been shown to characterize these discontinuous solutions. Still, the resulting equations need to be supplemented by the appropriate constitutive relations for the stresses and the fluid content. In particular, these relations must be developed for the localized quantities on $\boldsymbol{\Gamma}$, namely, for $\boldsymbol{t}_{\Gamma_x}$ and $\tilde{M}$.

The development of these localized constitutive laws is undertaken in this section. More specifically, we show that a poro-plastic continuum model is consistent with localized relations along the discontinuity. These ideas are developed in Section 3.2 after summarizing in Section 3.1 a classical continuum poro-plastic model. The assumed continuum model considers an additive elastoplastic decomposition of both the strains and the fluid content fields in the infinitesimal range of interest herein. A complete account of this type of models, following the thermodynamically consistent approach first proposed in the pioneering work of BIOT [1941], can be found in COUSSY [1995]. An extension to the finite deformation range in the framework given by a multiplicative decomposition of the deformation gradient can be found in ARMERO [1998].

3.1. The continuum poro-elastoplastic model

The governing equations described in the previous section are supplemented by the constitutive model characterizing the response of the porous solid, that is, defining the total stresses $\boldsymbol{\sigma}$ in terms of the independent unknown fields M and the infinitesimal strains

$\boldsymbol{\varepsilon} \equiv \boldsymbol{\varepsilon}(\boldsymbol{u}_\mu)$ in the small scale Ω_x of the material. A general coupled elastoplastic model can be characterized in this context by the additive decompositions

$$\boldsymbol{\varepsilon} = \boldsymbol{\varepsilon}^e + \boldsymbol{\varepsilon}^p \qquad \text{and} \qquad M = M^e + M^p \,, \tag{3.1}$$

in elastic and plastic parts. The reversible response of the porous solid is then characterized by a stored energy function $W = \hat{W}(\boldsymbol{\varepsilon}^e, M^e, \alpha)$, in terms of the elastic parts of the strains and fluid content increment, and an extra set of internal variables characterizing, for example, the hardening/softening of the material. The analyses presented in this paper consider, for simplicity, the case of isotropic hardening determined by a single scalar internal variable α. Similarly, isothermal conditions are assumed.

A standard argument based on the imposition of a positive internal dissipation (known as Coleman's method; see, e.g., TRUESDELL & NOLL [1965])

$$\mathcal{D}_{int} = \boldsymbol{\sigma}\!:\dot{\boldsymbol{\varepsilon}} + \mu_w \, \dot{M} - \dot{W} \geq 0 \,, \tag{3.2}$$

where the first term in the right-hand side of this expression accounts for the stress power and the second term for the change of internal energy due to fluid transport (the dissipation associated to fluid conduction is defined separately), leads to the constitutive relations

$$\boldsymbol{\sigma} = \partial_{\boldsymbol{\varepsilon}^e} W \,, \qquad \mu_w = \partial_{M^e} W \qquad \text{and} \qquad q = -\partial_\alpha W \,, \tag{3.3}$$

for total stresses $\boldsymbol{\sigma}$, the chemical potential of the fluid μ_w and the stress-like hardening internal variable q. The internal dissipation (3.2) can then be expressed equivalently as

$$\mathcal{D}_{int} = \boldsymbol{\sigma}\!:\dot{\boldsymbol{\varepsilon}}^p + \mu_w \, \dot{M}^p + q \, \dot{\alpha} \geq 0 \,, \tag{3.4}$$

as a straightforward calculation shows.

The rate forms of the constitutive relations (3.3) are given by

$$\dot{\boldsymbol{\sigma}} = \dot{\boldsymbol{\sigma}}' - b\rho_{wo}\dot{\mu}_w \, \boldsymbol{c} \,, \qquad \text{with} \qquad \dot{\boldsymbol{\sigma}}' = \mathbb{C}_{sk}\dot{\boldsymbol{\varepsilon}}^e \,, \tag{3.5}$$

for the *effective Biot's stresses* $\boldsymbol{\sigma}'$, and

$$\dot{\mu}_w = \dot{p}/\rho_w = \frac{Q}{\rho_{wo}^2}\left[\dot{M}^e - b\rho_{wo} \, \dot{\boldsymbol{\varepsilon}}^e : \boldsymbol{c}\right] \,, \tag{3.6}$$

for the fluid's chemical potential. Here, we have introduced the notation $\mathbb{C}_{sk}$ for the solid's skeleton elastic tangent ("drained" tangent), ρ_{wo} for the fluid's reference density, Q for the Biot's modulus, b for the Biot's coefficient, and $\boldsymbol{c}$ for the coupling tangent tensor. In particular, the linear elastic response is recovered through the quadratic stored energy function

$$W(\boldsymbol{\varepsilon}^e, M^e, \alpha) = \tfrac{1}{2}\boldsymbol{\varepsilon}^e : \mathbb{C}_u\boldsymbol{\varepsilon}^e + \frac{Q}{2\rho_{wo}^2}M^{e2} - \frac{bQ}{\rho_{wo}}\boldsymbol{\varepsilon}^e : \boldsymbol{c} \, M^e + H(\alpha) \,, \tag{3.7}$$

for a general hardening potential $H(\alpha)$ and the "undrained" material tangent $\mathbb{C}_u$ given in terms of the drained elasticities $\mathbb{C}_{sk}$ by

$$\mathbb{C}_u = \mathbb{C}_{sk} + Qb^2 \boldsymbol{c} \otimes \boldsymbol{c} \,. \tag{3.8}$$

The isotropic case is recovered with the choices

$$\mathbb{C}_{sk} = \kappa_{sk} \mathbf{1} \otimes \mathbf{1} + 2\mu_{sk} \left(\mathbb{I} - \frac{1}{3} \mathbf{1} \otimes \mathbf{1} \right) \qquad \text{and} \qquad \boldsymbol{c} = \mathbf{1} \,, \tag{3.9}$$

for the drained bulk κ_{sk} and shear μ_{sk} moduli, and the rank two $\mathbf{1}$ and rank four $\mathbb{I}$ identity tensors, respectively. The undrained tangent $\mathbb{C}_u$ possesses then the same form $(3.9)_1$, but with the undrained bulk modulus $\kappa_u = \kappa_{sk} + Qb^2$.

The evolution of the plastic internal variables $\boldsymbol{\varepsilon}^p$, M^p and α is given by the rate equations

$$\left.\begin{aligned} &\dot{\boldsymbol{\varepsilon}}^p = \lambda \, \partial_{\boldsymbol{\sigma}} f \,, \\ &\dot{\alpha} = \lambda \, \partial_q f \,, \\ &\dot{M}^p = \lambda \, \partial_{\mu_w} f \quad (= \lambda \rho_w \partial_p f) \,, \end{aligned}\right\} \tag{3.10}$$

for the associate case based on a yield surface $f(\boldsymbol{\sigma}, \mu_w(p), q)$. Equations (3.10) can be derived from the principle of maximum plastic dissipation, after following a standard argument based on (3.4). The plastic consistency parameter λ has been introduced in (3.10), and it is determined by the Kuhn-Tucker and consistency conditions

$$f \leq 0 \,, \quad \lambda \geq 0 \,, \quad \lambda f = 0 \,, \quad \text{and} \quad \lambda \dot{f} = 0 \,. \tag{3.11}$$

defining the loading/unloading conditions.

A common example of the above considerations is furnished by a yield condition $f(\boldsymbol{\sigma}, p, q) = f_{sk}(\boldsymbol{\sigma}', q)$ defined in terms of the effective stresses (3.5) (that is, characterizing the drained response of the porous solid). This choice leads to the relations

$$\partial_{\boldsymbol{\sigma}} f = \partial_{\boldsymbol{\sigma}'} f_{sk} \,, \qquad \text{and} \qquad \partial_p f = b \frac{\rho_{wo}}{\rho_w} \, \partial_{\boldsymbol{\sigma}'} f_{sk} : \boldsymbol{c} \,, \tag{3.12}$$

as a simple calculation based on the chain rule shows. In this case, equation $(3.10)_3$ reads

$$\dot{M}^p = \rho_{wo} \, b \, \boldsymbol{\varepsilon}^p : \boldsymbol{c} \quad (= \rho_{wo} \, b \, \dot{\varepsilon}^p_v \,, \quad \text{for the isotropic case}) \tag{3.13}$$

a direct relation of the evolution of the irreversible part of the fluid content M^p with the plastic dilatancy of the solid's skeleton, as characterized in the isotropic case by the volumetric plastic strain

$$\varepsilon^p_v := \operatorname{tr} [\boldsymbol{\varepsilon}^p] \,, \tag{3.14}$$

for the usual trace operator tr[·]. Combining (3.6) with (3.13), we obtain the relation

$$\dot{M} = \frac{\rho_{wo}}{Q}\,\dot{p} + \rho_{wo}\, b\, \dot{\varepsilon}_v\ , \tag{3.15}$$

for the volumetric strain $\varepsilon_v := \mathrm{tr}[\boldsymbol{\varepsilon}]$. Here, we have assumed a constant fluid density $\rho_w = \rho_{wo}$ and the isotropic case of interest in the developments of the sections to follow.

3.2. The localized dissipative mechanism

We show in this section that the developments presented in Section 2 identifying the regularity of the different fields are consistent with the coupled poro-elastoplastic model described in Section 3.1. The final goal is the identification of a localized stress-displacement-fluid flow relation along the strong discontinuity. In this context, we consider a localized dissipative mechanism characterized by a localized plastic flow given by

$$\lambda = \tilde{\lambda}\ \delta_{\Gamma_x}\ . \tag{3.16}$$

The conditions developed below identify then necessary conditions for the appearance of this assumed mechanism (see ARMERO & GARIKIPATI [1996]). The derivation involves basically the same arguments as in the developments presented in SIMO et al [1993], and proceeds as follows.

The traction vector $\boldsymbol{t}_{\Gamma_x} = \boldsymbol{\sigma}\boldsymbol{n}$ remains continuous by equilibrium, implying that $\dot{\boldsymbol{t}}_{\Gamma_x}$ is a regular function. After using (3.5) and the decomposition of the strains (2.9) in regular and singular parts, the rate of the traction can be written as

$$\begin{aligned}\dot{\boldsymbol{t}}_{\Gamma_x} = \dot{\boldsymbol{\sigma}}\boldsymbol{n} &= [\mathbb{C}_{sk}\dot{\boldsymbol{\varepsilon}}^e - \rho_{wo} b \dot{\mu}_w \mathbf{c}]\,\boldsymbol{n} \\ &= \underbrace{[\mathbb{C}_{sk}(\dot{\bar{\boldsymbol{\varepsilon}}} - \dot{\bar{\boldsymbol{\varepsilon}}}^p) - \rho_{wo} b \dot{\mu}_w \mathbf{c}]\,\boldsymbol{n}}_{regular} + \underbrace{\Big[\mathbb{C}_{sk}\Big((\dot{\boldsymbol{\xi}}\otimes\boldsymbol{n})^s - \tilde{\lambda}\partial_{\boldsymbol{\sigma}} f\Big)\Big]\,\boldsymbol{n}\ \delta_{\Gamma_x}}_{singular}\ ,\end{aligned} \tag{3.17}$$

noting again the regularity of the fluid chemical potential; see Remark 2.1. The regularity of the traction rate $\dot{\boldsymbol{t}}_{\Gamma_x}$ implies then that the singular part of (3.17) vanishes, that is,

$$\boldsymbol{Q}_{sk}\dot{\boldsymbol{\xi}} = \tilde{\lambda}\ \mathbb{C}_{sk}\partial_{\boldsymbol{\sigma}} f\ \boldsymbol{n} \qquad \text{where} \qquad \boldsymbol{Q}_{sk} = \boldsymbol{n}\cdot\mathbb{C}_{sk}\cdot\boldsymbol{n}\ , \tag{3.18}$$

the elastic acoustic tensor of the solid's skeleton.

Furthermore, the consistency condition $(3.11)_3$ implies

$$\begin{aligned}0 = \dot{f} &= \partial_{\boldsymbol{\sigma}} f : \dot{\boldsymbol{\sigma}} + \partial_p f\ \dot{p} + \partial_q f\ \dot{q} \\ &= \underbrace{\partial_{\boldsymbol{\sigma}} f : [\mathbb{C}_{sk}(\dot{\bar{\boldsymbol{\varepsilon}}} - \dot{\bar{\boldsymbol{\varepsilon}}}^p) - \rho_{wo} b \dot{\mu}_w \mathbf{c}] + \partial_p f\ \dot{p} + \partial_q f\ \dot{q}}_{regular} \\ &\quad + \underbrace{\partial_{\boldsymbol{\sigma}} f : \mathbb{C}_{sk}\Big((\dot{\boldsymbol{\xi}}\otimes\boldsymbol{n})^s - \tilde{\lambda}\partial_{\boldsymbol{\sigma}} f\Big)\ \delta_{\Gamma_x}}_{singular}\ ,\end{aligned} \tag{3.19}$$

Each of the regular and singular parts of this last expression must vanish, leading to

$$\tilde{\lambda} = \frac{1}{\partial_{\boldsymbol{\sigma}} f : \mathbb{C}_{sk} \partial_{\boldsymbol{\sigma}} f} \partial_{\boldsymbol{\sigma}} f : \mathbb{C}_{sk} \left(\dot{\boldsymbol{\xi}} \otimes \boldsymbol{n} \right)^s \ , \tag{3.20}$$

for the singular part. Combining this last relation with (3.18) we obtain the final condition for the direction of the jump rate $\dot{\boldsymbol{\xi}} = \|\dot{\boldsymbol{\xi}}\| \boldsymbol{m}$ (with $\|\boldsymbol{m}\| = 1$)

$$\boldsymbol{Q}_{sk}^{ep} \boldsymbol{m} = 0 \qquad \text{where} \qquad \boldsymbol{Q}_{sk}^{ep} = \boldsymbol{n} \cdot \left[\mathbb{C}_{sk} - \frac{1}{\partial_{\boldsymbol{\sigma}} f : \mathbb{C}_{sk} \partial_{\boldsymbol{\sigma}} f} \mathbb{C}_{sk} \partial_{\boldsymbol{\sigma}} f \otimes \mathbb{C}_{sk} \partial_{\boldsymbol{\sigma}} f \right] \cdot \boldsymbol{n} \ , \tag{3.21}$$

the *drained* perfectly plastic acoustic tensor.

In addition, the above relations lead to the following localized softening law. Given the regularity of the different fields involved, the softening law $(3.10)_2$ needs to be understood in the distributional sense

$$\mathcal{H}^{-1} \dot{q} := -\dot{\alpha} = -\tilde{\lambda} \ \partial_q f \ \delta_{\Gamma_x} \qquad \Longrightarrow \qquad \mathcal{H}^{-1} = \tilde{\mathcal{H}}^{-1} \ \delta_{\Gamma_x} \ , \tag{3.22}$$

for a localized softening modulus $\tilde{\mathcal{H}}$. This last equation identifies also the evolution of the localized equivalent plastic strain

$$\dot{\tilde{\alpha}} = \tilde{\lambda} \ \partial_q f \ , \tag{3.23}$$

having units of displacement. The combination of (3.22), the regular part of the consistency condition (3.19) and the equation (3.20) leads to the following localized relation for the magnitude of the rate of the displacement jump

$$\|\dot{\boldsymbol{\xi}}\| = \frac{1}{\tilde{\mathcal{H}} \ \Xi_{sk}} \underbrace{\left[\partial_{\boldsymbol{\sigma}} f : \dot{\boldsymbol{\sigma}} + \partial_p f \ \dot{p} \right]}_{\partial_{\boldsymbol{\sigma}'} f_{sk} : \dot{\boldsymbol{\sigma}}'} \qquad \text{where} \qquad \Xi_{sk} = \frac{(\partial_q f)^2}{\partial_{\boldsymbol{\sigma}} f : \mathbb{C}_{sk} \partial_{\boldsymbol{\sigma}} f} \mathbb{C}_{sk} \partial_{\boldsymbol{\sigma}} f : (\boldsymbol{m} \otimes \boldsymbol{n}) \ , \tag{3.24}$$

with $\|\dot{\boldsymbol{\xi}}\| = 0$ when the right-hand-side of $(3.24)_1$ vanishes (that is, a rigid-plastic response along Γ_x).

Finally, the origin of the singular character of the fluid content M can be identified with the plastic (or irreversible) part M^p through $(3.10)_3$ given (3.16). In fact, using $(3.10)_3$ and (2.18) the following expression is obtained

$$\dot{\tilde{M}} = -[\![\boldsymbol{q}_w]\!] \cdot \boldsymbol{n} = \rho_{w0} b \underbrace{\|\dot{\boldsymbol{\xi}}\| \ \boldsymbol{m} \cdot \boldsymbol{n}}_{\dot{\boldsymbol{\xi}} \cdot \boldsymbol{n}} \ , \tag{3.25}$$

for the singular part of the fluid content $\tilde{M}$, and from (3.15)

$$\dot{\tilde{M}} = \frac{\rho_{wo}}{Q} \ \dot{p} + \rho_{wo} \ b \ \dot{\tilde{\varepsilon}}_v \ , \tag{3.26}$$

for the regular fluid content increment. Equation (3.25) clearly indicates the relation of the localized fluid content $\tilde{M}$ with the dilatancy associated with the strong discontinuity, that is, the component of the displacement jump normal to the discontinuity.

In summary, the developments in this section show the consistency of a classical continuum poro-plastic model with localized relations along the strong discontinuities. In particular, the localized softening law (3.24), involving a stress/displacement relation, has been obtained. Similarly, the evolution of the localized fluid content in the fully saturated porous media is given by (3.25) through the dilatant response of the strong discontinuity. We consider in the next section the particular case of a dilatant shear layer to illustrate the significance of these localized relations.

Remark 3.1. The developments presented in this section have considered a general poro-plastic model, leading to a set of rigid-plastic relations along the discontinuity. As indicated in Section 1, we understand the developments presented herein as a motivation for the form of the final localized relations. The consistency of these localized laws with the original local continuum model is the main focus. Additional considerations (viscous effects, elastic unloading with or without damage, for example) can be incorporated in a more general framework as presented in ARMERO [1997a,b]. □

4. Model Problem: a Dilatant Shear Layer

As a model example of the considerations presented in the previous sections, we examine in this section the problem of an infinite shear layer. This model problem is defined as follows. We denote by L the thickness of the layer in the direction x, perpendicular to the layer, so $\Omega = [0, L] \subset \mathbb{R}$ in this case. We denote by $\boldsymbol{n} = [1 \quad 0]^T$ the unit vector in the x-direction and by $\boldsymbol{s} = [0 \quad 1]^T$ the unit vector in the perpendicular direction; see Figure 4.1 for an illustration of the notation. The layer is subjected to the normal and shear strains

$$\varepsilon_n = \frac{du_n}{dx} \qquad \text{and} \qquad \gamma_s = \frac{du_s}{dx} \,, \tag{4.1}$$

for the normal and shear displacements $u_n(x)$ and $u_s(x)$, respectively. In this setting, the total normal stress σ and the shear stress τ act on the layer at $x = L$ and are constant in Ω. The effective normal stress corresponding to σ is denoted by $\sigma' = \sigma + bp$. The material is assumed isotropic and characterized by a scalar permeability k (i.e., $\boldsymbol{k} = k\,\mathbf{1}$), so the fluid flow q_w is in the x-direction by symmetry. Gravity effects are neglected, and a constant fluid density $\rho_w = \rho_{wo}$ is assumed.

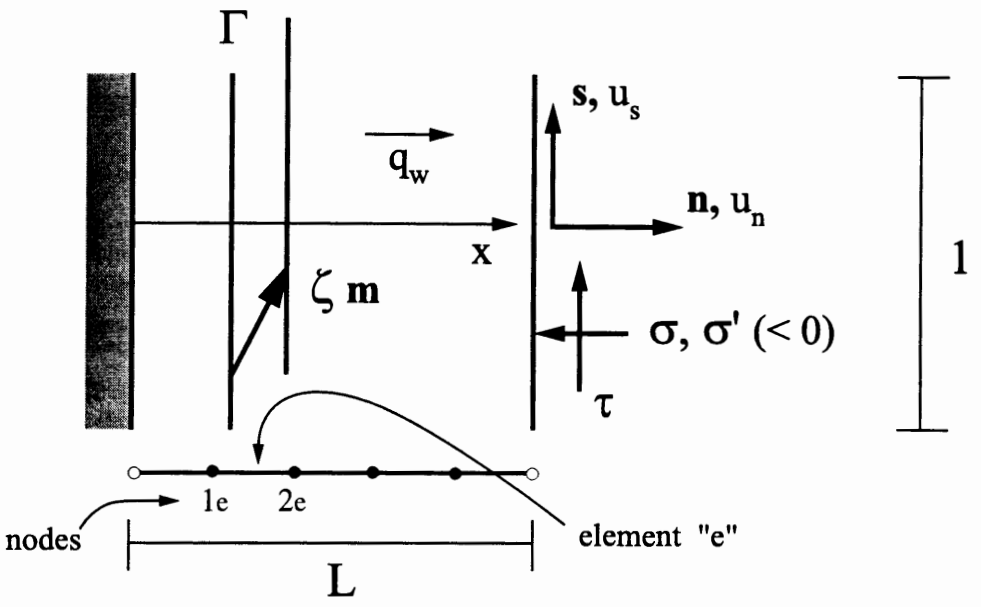

FIGURE 4.1. Dilatant shear layer. Problem definition illustrating the notation for the normal and shear components of the displacement and stress, the fluid flow, and the finite element discretization.

4.1. The poro-elastoplastic model

The poro-elasto-plastic model described in Section 3.1 reduces in this case to the following equations. First, we consider the linear elastic stress-strain laws

$$\dot{\sigma}' = E_{oe}\,(\dot{\varepsilon}_n - \dot{\varepsilon}_n^p) \qquad \text{and} \qquad \dot{\tau} = G\,(\dot{\gamma}_s - \dot{\gamma}_s^p)\ , \tag{4.2}$$

for the oedometric modulus E_{oe} and the shear modulus G. The Mohr-Coulomb yield criterion

$$f_{sk}\,(\tau, \sigma', \alpha) = |\tau| + \beta\sigma' - q\,(\alpha)\ , \tag{4.3}$$

is assumed for the elastoplastic response, where $\beta = \tan\varphi$ for the drained friction angle φ, and $q(0)$ $(= c)$ is the initial drained cohesion of the material. The continuum plastic evolution equations (3.10) read in this case

$$\dot{\varepsilon}_n^p = \lambda\ \beta\ , \qquad \dot{\gamma}_s^p = \lambda\ \text{sign}\,(\tau)\ , \qquad \dot{\alpha} = \lambda \qquad \text{and} \qquad \dot{M}^p = \rho_{wo}\ \dot{\varepsilon}_n^p\ . \tag{4.4}$$

The loading/unloading and consistency conditions (3.11) are added to these equations.

The combination of equations (4.2) to (4.4) leads to the following rate form of the assumed continuum poro-plastic model

$$\begin{Bmatrix} \dot{\sigma}' \\ \dot{\tau} \end{Bmatrix} = \underbrace{\frac{1}{G + \beta^2\ E + \mathcal{H}} \begin{bmatrix} E(G + \mathcal{H}) & -\beta\ E\ G\ \text{sign}(\tau) \\ -\beta\ E\ G\text{sign}(\tau) & G(\beta^2\ E + \mathcal{H}) \end{bmatrix}}_{\mathbb{C}_{sk}^{ep}} \begin{Bmatrix} \dot{\varepsilon}_n \\ \dot{\gamma}_s \end{Bmatrix}\ , \tag{4.5}$$

in terms of the continuum hardening/softening modulus $\mathcal{H} := -dq(\alpha)/d\alpha$. The so-called dilatant hardening can be observed in the term involving the $\mathcal{H} + \beta^2 E$ combination. Still, the perfectly plastic case $\mathcal{H} = 0$ leads to a singular tangent $\mathbb{C}^{ep}_{sk}$ with the eigenvector corresponding to the zero eigenvalue given by

$$\boldsymbol{\varepsilon}^{eig} = \left\{ \begin{array}{c} \dot{\varepsilon}_n^{eig} \\ \dot{\gamma}_s^{eig} \end{array} \right\} = \frac{1}{\sqrt{1+\beta^2}} \left\{ \begin{array}{c} \beta \\ \text{sign}(\tau) \end{array} \right\} . \tag{4.6}$$

This strain mode can be written as a the symmetric part of the rank one update (in the particular notation employed in (4.6) for the strain rate vector) as

$$\dot{\boldsymbol{\varepsilon}}^{eig} \longleftarrow \text{sym}\,(\boldsymbol{m} \otimes \boldsymbol{n}) \qquad \text{for} \qquad \boxed{\boldsymbol{m} = [\![\boldsymbol{u}]\!]/\|[\![\boldsymbol{u}]\!]\| = \frac{1}{\sqrt{1+\beta^2}} \left[\beta\, \boldsymbol{n} + \text{sign}(\tau)\, \boldsymbol{s}\right] ,} \tag{4.7}$$

thus corresponding also to the condition (3.21) based on the acoustic tensor $\boldsymbol{Q}^{ep}_{sk}$. Therefore, the localization condition (3.21) is satisfied upon yielding, with the normal $\boldsymbol{n}$ to the strong discontinuity surface at x_Γ given by the normal to the layer, and the constant direction $\boldsymbol{m}$ of the displacement jump given by (4.7). The dilatant character of the discontinuity jump, as reflected by the normal component of the strain mode $\boldsymbol{\varepsilon}^{eig}$, is apparent for $\beta \neq 0$.

Remark 4.1. We note that the conclusion that the dilatant shear layer loses its stability when the underlying drained elastoplastic model reaches the softening range agrees completely with the analysis presented in RICE [1975] for this very same model example. In this reference, a complete linearized stability analysis of the governing equations, including the conservation of fluid mass through Darcy's law, is presented. This analysis identifies the short-wavelength limit as leading to the observed instability, with no intrinsic length-scale present in this shear problem. □

Following the analysis of Section 3.2 characterizing the resulting strong discontinuities, the strain rates are decomposed upon localization in a regular and a singular parts, namely

$$\dot{\varepsilon}_n = \dot{\bar{\varepsilon}}_n + \dot{\xi}_n\, \delta_{\Gamma_x} \qquad \text{and} \qquad \dot{\gamma}_s = \dot{\bar{\gamma}}_s + \dot{\xi}_s\, \delta_{\Gamma_x} , \tag{4.8}$$

where

$$\dot{\xi}_n = \dot{\boldsymbol{\xi}} \cdot \boldsymbol{n} = \dot{\xi} \frac{\beta}{\sqrt{1+\beta^2}} \qquad \text{and} \qquad \dot{\xi}_s = \dot{\boldsymbol{\xi}} \cdot \boldsymbol{s} = \dot{\xi}\, \frac{\text{sign}(\tau)}{\sqrt{1+\beta^2}} , \tag{4.9}$$

are the normal and the shear components of the displacement jump rate, respectively. The magnitude of the rate of the jump $\dot{\xi}$ is given by the localized relation (3.24), which reads in this case

$$\dot{\tau}\, \text{sign}\,(\tau) + \beta\, \dot{\sigma}' = \frac{\tilde{\mathcal{H}}}{\sqrt{1+\beta^2}} \dot{\xi} . \tag{4.10}$$

A constant softening modulus $\tilde{\mathcal{H}}$ (i.e., linear softening) is assumed in the simulations of Section 5. The localized fluid content in Γ_x, given by (3.25), reads in this case

$$\dot{\tilde{M}} = -[\![q_w]\!] = \frac{\rho_{wo}\, b\, \beta}{\sqrt{1+\beta^2}}\, \dot{\xi}\ , \tag{4.11}$$

in terms of the constant fluid density ρ_{wo}, the Biot's coefficient b and the dilatancy factor β. Similarly, the regular part of the fluid content increment, given by equation (3.26), can be written for the current case of interest

$$\dot{\bar{M}} = \frac{\rho_{wo}}{Q}\, \dot{p} + \rho_{wo}\, b\, \dot{\bar{\varepsilon}}_n\ , \tag{4.12}$$

for the Biot's modulus Q and the regular part of the normal strain $\bar{\varepsilon}_n$.

4.2. An enhanced finite element formulation

The above considerations are implemented in the context of enhanced strain finite element methods, following the formulations presented in ARMERO & GARIKIPATI [1995,96] which do not resort to the regularization of the singular Dirac delta functions. In this geometrical one-dimensional setting, we consider the isoparametric interpolation of the large-scale displacement fields u_n and u_s

$$u_n(x) = \boldsymbol{N}_e(x)\boldsymbol{d}_{n_e} \quad \text{and} \quad u_s(x) = \boldsymbol{N}_e(x)\boldsymbol{d}_{s_e} \quad \text{for} \quad x \in \Omega_e\ , \tag{4.13}$$

for the piece-wise linear shape functions

$$\boldsymbol{N}_e(x) = \begin{bmatrix} -(x - x_{2e})/h_e \\ (x - x_{1e})/h_e \end{bmatrix}\ , \tag{4.14}$$

for a typical two-node element $\Omega_e = [x_{1e}, x_{2e}] \subset \Omega = [0, L]$ (with $h_e = |x_{2e} - x_{1e}|$) in terms of the nodal displacements vectors $\boldsymbol{d}_{n_e}$ and $\boldsymbol{d}_{s_e}$, for the normal and shear displacements, respectively. The strain field is approximated through the enhanced strategy

$$\varepsilon_{n_e} = \underbrace{\boldsymbol{B}_e\boldsymbol{d}_{n_e} - \frac{1}{h_e}\xi_{n_e}}_{\bar{\varepsilon}_{n_e}} + \xi_{n_e}\, \delta_{\Gamma_x}\ , \qquad \text{and} \qquad \gamma_{s_e} = \underbrace{\boldsymbol{B}_e\boldsymbol{d}_{s_e} - \frac{1}{h_e}\xi_{s_e}}_{\bar{\gamma}_{n_e}} + \xi_{s_e}\, \delta_{\Gamma_x}\ , \tag{4.15}$$

in the elements where localization is detected, where

$$\boldsymbol{B}_e := \nabla \boldsymbol{N}_e = \frac{1}{h_e}\begin{bmatrix} -1 & 1 \end{bmatrix}\ , \tag{4.16}$$

the standard strain matrix associated to the conforming part of the displacements (the large-scale strain field in the notation of Section 2). The scalars ξ_{n_e} and ξ_{s_e} correspond to

a constant approximation over the element of the normal and shear displacement jumps, respectively, and are given in terms of a single enhanced parameter ξ_e for element Ω_e through the relations (4.9).

The enhanced interpolation (4.15) of the strains can be understood as arising from the displacement interpolation

$$\boldsymbol{u}_\mu(x) = \boldsymbol{N}_e(x)\boldsymbol{d}_e + \boldsymbol{\xi}_e\, \Psi_{\Gamma e}(x) \qquad x \in [x_{1e}, x_{2e}] \ , \tag{4.17}$$

for $\boldsymbol{d}_e = [\, \boldsymbol{d}_{n_e} \quad \boldsymbol{d}_{s_e}\,]^T$ and $\boldsymbol{\xi}_e = [\, \xi_{n_e} \quad \xi_{s_e}\,]^T$, in terms of the interpolating function

$$\Psi_{\Gamma e}(x) = H_{x_{\Gamma e}}(x) - N_{2e}(x) \ , \tag{4.18}$$

for the shape function $N_{2e}(x)$ in $(4.14)_2$ and the Heaviside function $H_{x_{\Gamma e}}(x)$ exhibiting a unit jump across the discontinuity at the center of the element

$$x_{\Gamma e} = \tfrac{1}{2}\,(x_{2e} + x_{1e}) \ . \tag{4.19}$$

The function $\Psi_{\Gamma e}(x)$ is depicted in Figure 4.2, and corresponds to an approximation of the function $\psi_\Gamma(x)$ in (2.7) as employed in the developments of Section 2.2 for the continuum problem. The relation

$$\int_{x_{1e}}^{x_{2e}} \Psi_{\Gamma e}(x)\ dx = 0 \ , \tag{4.20}$$

over an element Ω_e is satisfied, in particular. The multi-scale framework developed in Section 2 clearly applies to the proposed finite element method with simply identifying the local neighborhood Ω_x with the element Ω_e for the material point x_Γ. We note, however, that the entire formulation only makes use of the enhanced strain as written in (4.15). As obtained in the previous section for the one-dimensional problem at hand, a strong discontinuity is activated upon yielding.

The final governing equations for the mechanical problem consist of the principle of virtual work equation (2.3) of the large-scale problem for $\boldsymbol{u}$, and the localized equilibrium relation (2.11). For the problem at hand, the weak form (2.3) reduces to the set of residual equations

$$\left.\begin{aligned} \boldsymbol{R}_n &:= \boldsymbol{f}_{n_{ext}} - \mathop{\mathbf{A}}_{e=1}^{n_{elem}} \int_{x_{1e}}^{x_{2e}} \boldsymbol{B}_e^T \sigma\ dx = 0 \ , \\ \boldsymbol{R}_s &:= \boldsymbol{f}_{s_{ext}} - \mathop{\mathbf{A}}_{e=1}^{n_{elem}} \int_{x_{1e}}^{x_{2e}} \boldsymbol{B}_e^T \tau\ dx = 0 \ , \end{aligned}\right\} \tag{4.21}$$

for normal and shear external nodal force components $\boldsymbol{f}_{n_{ext}}$ and $\boldsymbol{f}_{s_{ext}}$, respectively, including imposed boundary displacements. The symbol $\mathbf{A}$ has been used in (4.21) to denote the assembly of all the n_{elem} element contributions. The stresses σ and τ are obtained

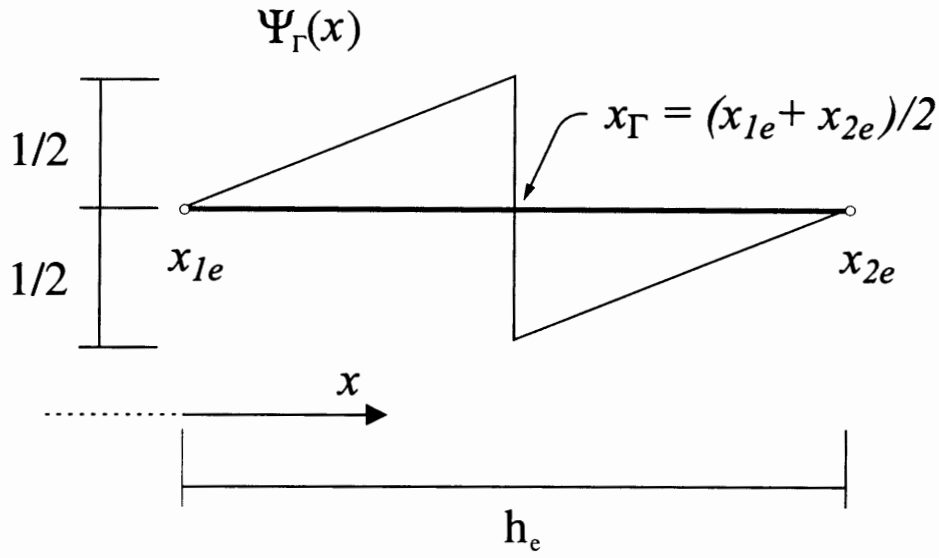

FIGURE 4.2. Dilatant shear layer. One-dimensional enhanced finite element with a discontinuous shape function at the mid-point $x_{\Gamma e} = (x_{1e} + x_{2e})/2$.

trough the elastic relations (4.2) for the effective stresses, in terms of the regular part of the strains $\bar{\varepsilon}_n$ and $\bar{\gamma}_s$, respectively, in (4.15), and the pressure contribution discussed below. The corresponding integrals are evaluated through a single quadrature point at the center of the element.

The localized equilibrium relation (2.11) reduces in this case, involving a constant approximation of the displacement jumps over the element, to the nonlinear scalar relation

$$\boxed{\left.\begin{array}{ll} |\tau| + \beta\sigma' - \tilde{q}(\xi_e) = 0\,, & \text{for} \quad \dot{\xi}_e > 0\,, \\ \xi_e = \text{constant}, & \text{otherwise}\,, \end{array}\right\}} \tag{4.22}$$

after using the localized softening relation (4.10), in terms of the stresses $\{\sigma, \tau\}$ and the localized softening stress-displacement law $\tilde{q}(\xi_e)$ (note that, in this case, $\tilde{\alpha} = \xi_e$ as defined in (3.23)). The rate form of (4.22) is given by equation (4.10). The normal ξ_{n_e} and shear ξ_{s_e} components of the jump are obtained in terms of ξ_e through the constant relations (4.9). The integration of the localized equations (4.22) follows the same steps as described in ARMERO & GARIKIPATI [1995].

The fluid flow contributions are interpolated using a similar piece-wise linear interpolation of the pore pressure field p, that is,

$$p(x) = \boldsymbol{N}_e(x)\boldsymbol{p}_e \qquad \text{for} \quad x \in \Omega_e = [x_{1e}, x_{2e}]\,, \tag{4.23}$$

and the same shape functions $\boldsymbol{N}_e$ as in $(4.14)_2$ for the nodal pore pressure parameters $\boldsymbol{p}_e = [\,p_{1e} \quad p_{2e}\,]^T$. The weak form of the fluid mass balance equation (2.24) leads in this case to

$$\int_0^L \dot{\tilde{M}}\ \delta p\ dx + \sum_{e=1}^{n_{loc}} \dot{\tilde{M}}_e\ \delta p(x_{\Gamma e}) = \int_0^L q_w\ \frac{d}{dx}\,(\delta p)\ dx - [q_w\ \delta p]_0^L\ , \tag{4.24}$$

for all admissible variations $\delta p \in \mathcal{V}_p$ and for n_{loc} elements exhibiting a strong discontinuity. Consistent with the one-point quadrature assumed for the mechanical contributions and the mid-point location of the discontinuity $x_{\Gamma e}$ in (4.19), the contribution of the localized fluid content involves simply $\delta p(x_{\Gamma e}) = (\delta p_{1e} + \delta p_{2e})/2$ for the assumed linear pressure interpolation. Alternative locations of the discontinuity in an element can be considered; details are omitted.

The presence of the localized flow $\dot{\tilde{M}}_e = -[\![q_w]\!]_e$ appears as an added source term to the fluid mass balance, and it is given by the relation (4.11) in terms of the displacement jump rate $\dot{\xi}_e$. The associated discontinuity of the fluid flow q_w is incorporated at the element level through an *enhancement* of the conforming contribution of the gradient of the assumed linear pressure interpolation. More precisely, we consider at the element level the enhanced interpolation

$$q_w\,(x) = -\rho_{wo} k\,\boldsymbol{B}_e\,\boldsymbol{p}_e + [\![q_{w_e}]\!]\ \Psi_{\Gamma e}\,(x) \qquad x \in [x_{1e}, x_{2e}]\ , \tag{4.25}$$

for the conforming gradient operator $\boldsymbol{B}_e$ defined in (4.16). Noting the property (4.20) for the discontinuous interpolation function $\Psi_{\Gamma e}(x)$ and the constant character of the pore pressure gradient variations $d(\delta p)/dx$, we observe that the fluid flow jump $[\![q_w]\!]$ is effectively eliminated from the balance equation (4.24). The actual value of $[\![q_w]\!]$ is obtained from the localized relation (4.11) as a post-processing, if desired. Similar to the enhancement of the strains discussed above, the discontinuous contribution to the fluid flow vector in (4.25) can be understood as arising from an enhanced interpolation of the pressure field, incorporating the continuous function

$$\Psi^p_{\Gamma e}(x) := \int_{x_{1e}}^{x} \Psi_{\Gamma e}(\eta)\ d\eta \qquad x \in [x_{1e}, x_{2e}]\ , \tag{4.26}$$

exhibiting a discontinuity in the first derivative at $x_{\Gamma e}$. Note that, given (4.20), we have the property

$$\Psi^p_{\Gamma e}(x_{1e}) = \Psi^p_{\Gamma e}(x_{2e}) = 0$$

thus defining an added hierarchic interpolation to the original linear pressure interpolation. The numerical results reported in Section 5 do not use, however, this alternative more complex post-processing when reporting the spatial distributions of the pore pressure.

The final discrete system of equations corresponding to the fluid mass conservation (4.24) is obtained by considering the constitutive relations (4.12) and (4.11) for the regular

and singular parts, respectively, of the fluid content increment. In particular, for the one-dimensional finite element interpolations considered in this section, equation (4.12) can be written as

$$\begin{aligned}\dot{\tilde{M}}\Big|_{\Omega_e} &= \frac{\rho_{wo}}{Q}\,\dot{p} + \rho_{wo}\,b\,\dot{\bar{\varepsilon}}_n \\ &= \frac{\rho_{wo}}{Q}\,\dot{p} + \rho_{wo}\,b\,\left(\dot{\varepsilon}_n - \frac{1}{h_e}\dot{\xi}_e\right) \\ &= \frac{\rho_{wo}}{Q}\,\dot{p} + \rho_{wo}\,b\,\dot{\varepsilon}_n - \frac{1}{h_e}\,\dot{\tilde{M}}_e \qquad \text{in} \quad \Omega_e\end{aligned} \tag{4.27}$$

after using (4.11) and $(4.15)_1$. Given the relation

$$\delta p(x_{\Gamma e}) = \frac{1}{h_e}\int_{x_{1e}}^{x_{2e}} \delta p(x)\,dx\,, \tag{4.28}$$

for the assumed mid-point location (4.19) of $x_{\Gamma e}$, we observe then that the introduction of the relation (4.27) in the weak equation (4.24) leads to the cancellation of the localized fluid content terms corresponding to $\dot{\tilde{M}}_e$, as a simple calculation shows. The resulting finite element equation reads

$$\boxed{\boldsymbol{S}\dot{\boldsymbol{p}} + \boldsymbol{Q}^T\dot{\boldsymbol{d}}_n + \boldsymbol{H}\boldsymbol{p} - \boldsymbol{r}_{ext} = \boldsymbol{0}\,,} \tag{4.29}$$

where we have introduced the notation

$$\begin{aligned}&\boldsymbol{S} := \mathop{\mathbf{A}}_{e=1}^{n_{elem}} \int_{\Omega_e} \frac{\rho_{wo}}{Q}\,\boldsymbol{N}_e^T\boldsymbol{N}_e\,dx\,, \qquad \boldsymbol{H} := \mathop{\mathbf{A}}_{e=1}^{n_{elem}} \int_{\Omega_e} \rho_{wo}k\,\boldsymbol{B}_e^T\boldsymbol{B}_e\,dx\,, \\ &\text{and} \quad \boldsymbol{Q} := \mathop{\mathbf{A}}_{e=1}^{n_{elem}} \int_{\Omega_e} \rho_{wo}b\,\boldsymbol{B}_e^T\boldsymbol{N}_e\,dx\,,\end{aligned} \tag{4.30}$$

and the vector of imposed external fluxes $\boldsymbol{r}_{ext}$, including the corresponding contributions of imposed boundary pressures. Physically, equation (4.29) imposes weakly the global (large-scale) balance of fluid mass as given by the regular contributions of the fluid flow fields, whereas the localized balance of fluid mass on the strong discontinuity is handled locally at the element level. For the assumed mid-point location of the discontinuity, the localized accumulation of fluid content $\tilde{M}$ in the discontinuity is a consequence of the strain $-\xi_{ne}/h_e$ associated to the normal displacement jump ξ_{ne} over the rest of the element, as relation (4.27) shows. This localized fluid content can then be obtained as a post-processing in terms of the enhanced parameter ξ_e through (4.11).

In summary, the proposed finite element formulation involves the assembly and numerical solution of the nonlinear system of discrete equations (4.21) and (4.29). The

TABLE 5.1. Material parameters for the poro-plasticity model considered in the numerical simulations presented herein.

Oedometric Modulus	E_{oe}	2700	kPa
Shear Modulus	G	770	kPa
Initial Cohesion	c	30	kPa
Frictional Parameter	β	0.45	
Permeability	k	$1 \cdot 10^{-8}$	$m^2/(kPa\ s)$
Biot's Modulus	Q	$3.33 \cdot 10^4$	kPa
Biot's Coefficient	b	1	
Fluid Density	ρ_{wo}	$1.0 \cdot 10^3$	kg/m^3

numerical simulations presented in Section 5 make use of a Newton-Raphson scheme to solve this coupled set of nonlinear equations, with the quasi-static equilibrium equations (4.21) imposed at the end of the time step and the evolution equations (4.29) discretized in time with a backward-Euler scheme. Equation (4.22) is employed for the solution of the local enhanced parameter ξ_e, and eliminated through its static condensation in the corresponding contributions of the stresses in the mechanical equations (4.21). We refer to ARMERO & GARIKIPATI [1995,96] for complete details on this procedure; details are omitted herein. The final formulation involves then a nonlinear discrete problem in the nodal displacements $\boldsymbol{d}_e$ and the nodal pressures $\boldsymbol{p}_e$ only, *the large-scale problem*, while incorporating effectively the effects of the localized dissipative mechanisms.

5. Representative Numerical Simulations

The purpose of this section is to evaluate the performance of the finite element formulation proposed in Section 4.2. To this purpose, we present the results obtained for two different problems involving the dilatant shear layer studied in Section 4. More specifically, Section 5.1 considers the undrained shear test, referring to the assumed impervious boundaries of the shear layer. In contrast, Section 5.2 considers the drained shear test characterized by an imposed pore pressure along the boundaries.

5.1. The undrained shear test

We first consider a layer $L = 0.63\ m$ thick with impervious boundaries at $x = 0$ and $x = L$. A constant normal stress of $\sigma = -200\ kPa$ is suddenly imposed at $t = 0$ and it is maintained constant during the test at $x = L$. The simulation is run by imposing a shear displacement at $x = L$, with a constant rate of $\dot{u}_s(L) = a = 4.0 \cdot 10^{-8}\ m/s$. Fixed boundary conditions are assumed at $x = 0$ leading to the shear of the layer. The assumed

material parameters have been included in Table 5.1. In particular, the Biot modulus Q has been computed by means of the relation

$$\frac{1}{Q} = \frac{\phi_0}{\kappa_w} + \frac{1-\phi_0}{\kappa_s} \tag{5.1}$$

where $\phi_0 = 0.3$ is the initial porosity, and $\kappa_w = 10^4\ kPa$ and $\kappa_s = 10^{16}\ kPa$ are the bulk moduli of the fluid and the solid phases, respectively. We consider a piece-wise linear finite element discretization of the problem, as described in Section 4.2, with a lumped form (row sum) of the capacity matrix $\boldsymbol{S}$. More specifically, we consider the enhanced finite element formulation presented in the previous section with the response in the discontinuity given by a linear localized softening law (4.22) with a localized softening modulus of $\tilde{\mathcal{H}} = -1000\ kPa/m$. We also perform numerical simulations involving standard isoparametric linear elements based on a continuum local model with strain softening modulus of $\mathcal{H} = -25\ kPa$.

The shear stress τ and the pore pressure p at the center versus the imposed shear displacement are depicted in Figure 5.1.a for the newly proposed enhanced finite element formulation and in Figure 5.1.b for the standard isoparametric finite elements. In both cases we can observe an initial elastic range, characterized by a linear increase of the shear stress τ (constant across the layer by equilibrium) versus the imposed shear strain γ_s together with a constant value of the pore pressure p and corresponding normal effective σ' and total σ stresses. Due to the assumed undrained boundary conditions in this test, no rate effects appear in this elastic solution.

To trigger the localization of the strain upon reaching yielding, an imperfection in the form of a 1% reduction of the initial cohesion c is introduced in the element at the center. The solutions thereafter involve a localized pattern, characterized by the activation of the enhanced parameters approximating the jump of the displacements for the simulations involving the enhanced finite elements. Computations are conducted with two different discretizations of the sample, involving 17 and 45 equally spaced finite elements, respectively. As observed in Figure 5.1.a, the response obtained with the two meshes coincides for the enhanced finite elements, verifying the lack of pathological mesh dependence of the proposed formulation. This situation is to be contrasted by the strong mesh dependence exhibited by standard isoparametric finite elements with continuum strain softening, as depicted in Figure 5.1.b.

Figures 5.2.a and 5.2.b include the distributions of the fluid content and the shear plastic strain, respectively, obtained with the enhanced finite element formulation for the 17 element mesh. The localization of the plastic strain at the center is apparent. Similarly, and due to the dilatant behavior of the discontinuity, the fluid content increases at the center, while it decreases in the adjacent material, leading to the observed localized pattern of the fluid content; see Figure 5.2.a. This kind of response is also shown in Figure 5.3 by the induced fluid flow depicting a jump across the strong discontinuity, with the fluid

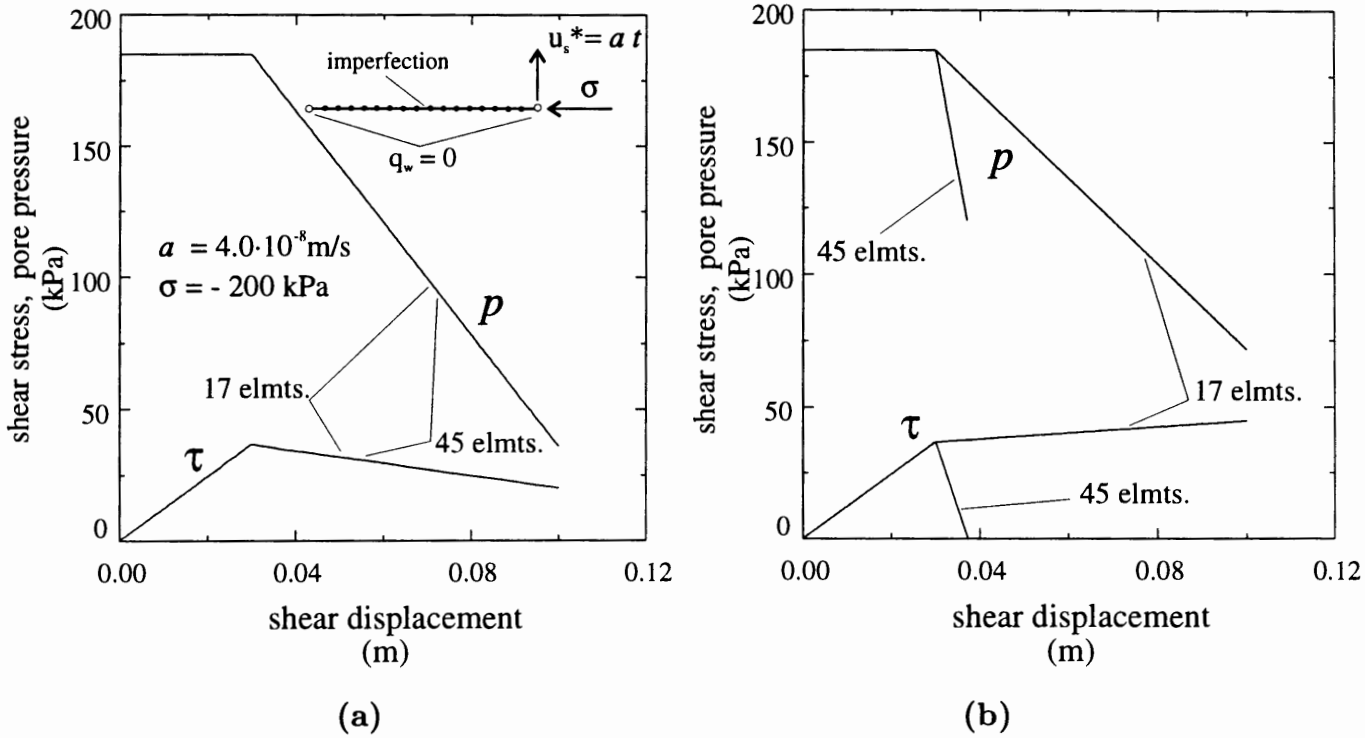

FIGURE 5.1. Shear layer of a dilatant material: undrained test. Shear stress and pore pressure at the center versus shear displacement: **(a)** Enhanced finite elements, and **(b)** standard isoparametric formulation.

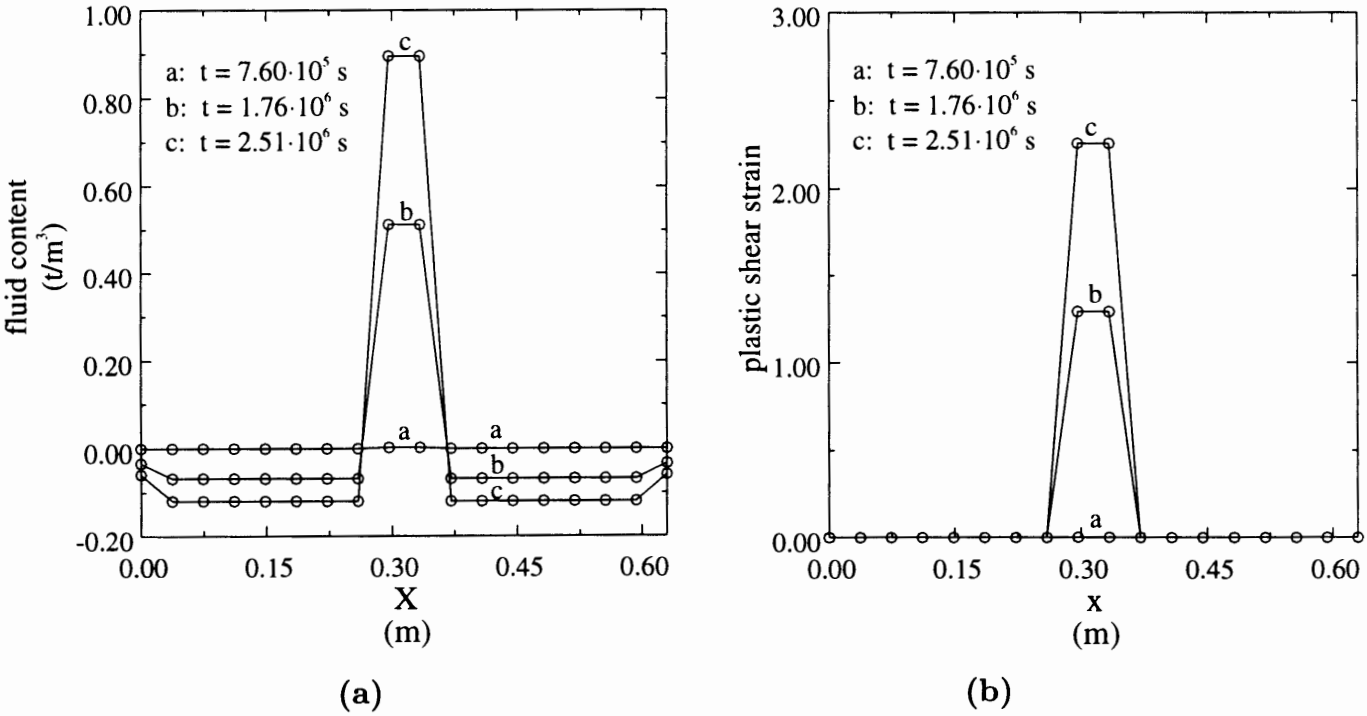

FIGURE 5.2. Shear layer of a dilatant material: undrained test. Isochrones of **(a)** fluid content, **(b)** plastic shear strain. Solution obtained with the enhanced finite element formulation with the 17 elements mesh; plots obtained with a lumped L_2 projection to the nodes.

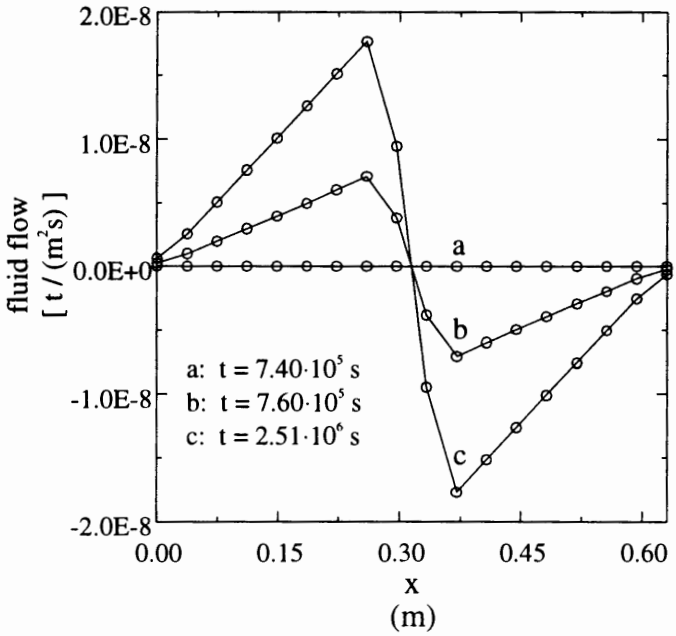

FIGURE 5.3. Shear layer of a dilatant material: undrained test. Isochrones of the fluid flow q_w. Solution obtained with the enhanced finite element formulation with the 17 elements mesh; plots obtained with a lumped L_2 projection to the nodes.

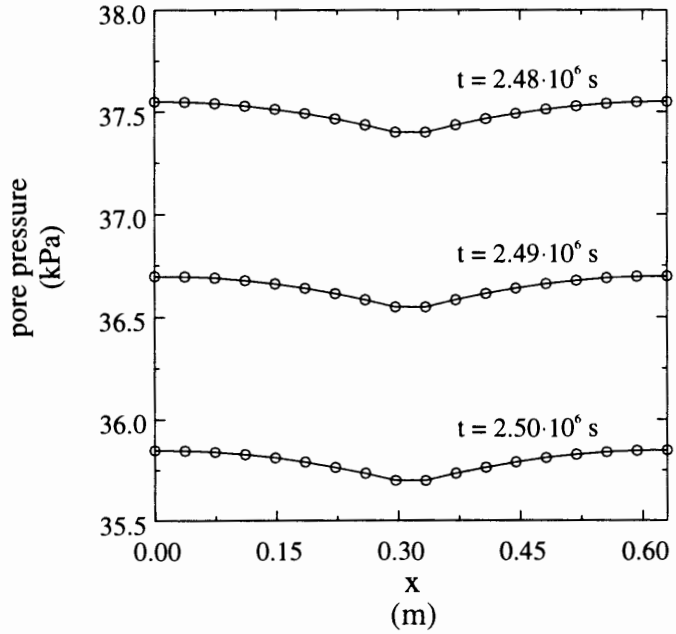

FIGURE 5.4. Shear layer of a dilatant material: undrained test. of the pore pressure p. Solution obtained with the enhanced finite element formulation with the 17 elements mesh.

flow on each side towards the discontinuity at the center. We note that these plots have been obtained with the use of a lumped L_2 projection of the values at the center of the elements to the nodes; the smooth distribution of the plastic quantities outside the central element is an artifact of this projection. The spatial distribution of the pore pressure along the sample is depicted in Figure 5.4 at different times for this solution. We can observe the decrease of the pore pressure at the center due to the presence of the dilatant strong discontinuity and the corresponding localized increase of the fluid content.

5.2. The drained shear test

We assume free draining boundaries at both ends in this second test. The same dimensions and material parameters summarized in Table 5.1 are employed in this case. The simulations are run also with an imposed shear displacement at $x = L$ after imposing a sudden initial normal stress of $\sigma = -200\ kPa$, which is also maintained constant during the simulations. The draining through the boundaries introduces in this case a non-constant distribution of the pore pressure, leading to rate-dependence even in the elastic range. The goal in this test is to study the influence of these effects in the resulting localization patterns. To this purpose, two constant strain rates $\dot{u}_s(L) = a$ of $a = 2.0 \cdot 10^{-5}\ m/s$ and $a = 6.0 \cdot 10^{-5}\ m/s$ are considered. The higher strain rates in this case are required for the yield in the specimen to occur before the total dissipation of the pore pressures.

As in the previous section, we consider simulations based on the proposed enhanced finite elements and standard isoparametric finite elements. A linear localized softening stress-displacement law of the form given in (4.22) is assumed in the former, with a localized modulus of $\tilde{\mathcal{H}} = -3000\ kPa/m$. The continuum strain softening modulus assumed in this test is $\mathcal{H} = -75\ kPa$. Spatial discretizations involving 9 and 17 piecewise linear elements in an equally spaced distribution are assumed.

Figure 5.5 depicts the evolution of the shear stress and the pore pressure at the center of the specimen versus the imposed shear strain. The rate-dependent effects are clear in these plots. Figure 5.6 depicts the pore pressure distribution for the enhanced finite element solution based on the 17 element mesh. The gradual dissipation of the pore pressure after an initial build up due to the applied constant normal stress can be observed in this figure, with its characteristic spatial distribution corresponding to one-dimensional elastic consolidation. Since the total normal compressive stress σ is maintained constant, the effective normal stress $\sigma' = \sigma + b\ p$ follows a similar distribution. Note that during the initial elastic stages the normal and shear components of the deformation process are entirely uncoupled, thus the applied shear strain has no effect on the fluid motion in this range.

The specimen eventually yields at the center. To avoid the strong numerical sensitivity that we have observed in capturing this yielding at the exact center, we also consider in this case a 1% reduction of the initial cohesion c at the center element. The plastic

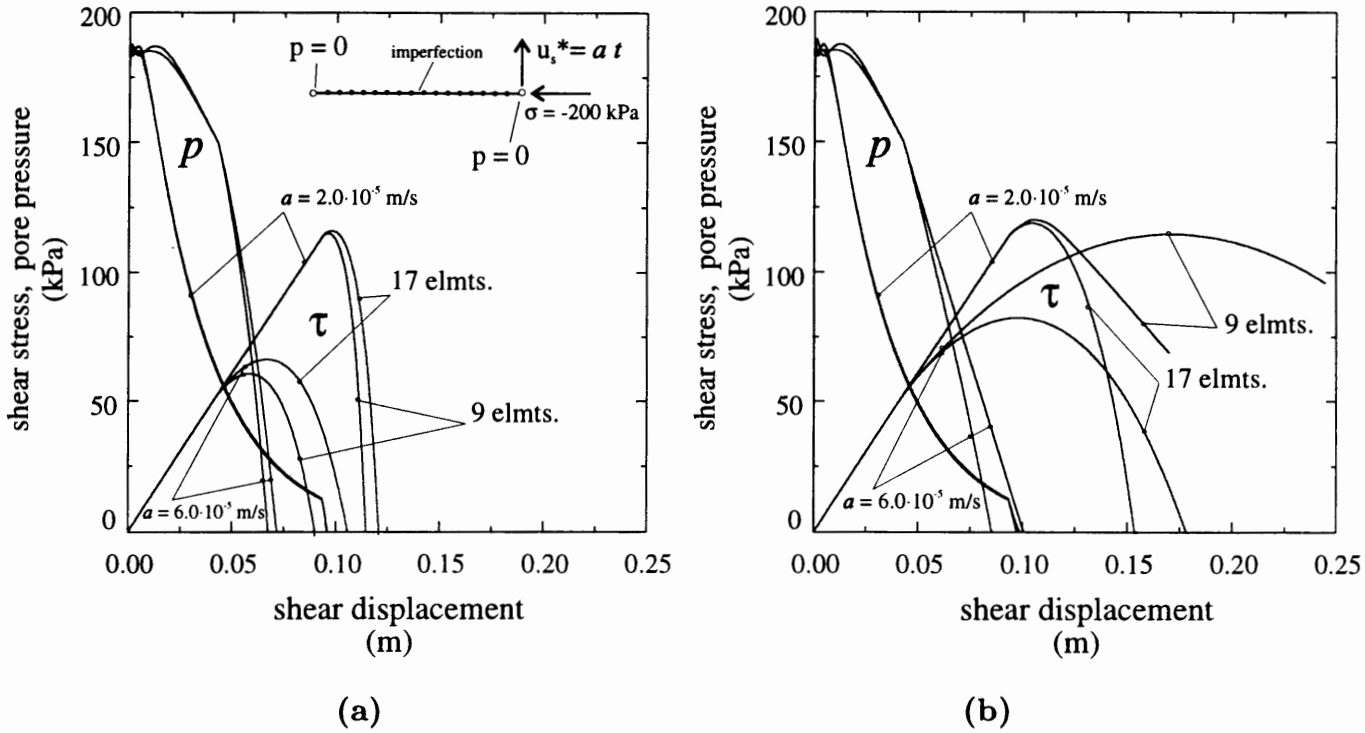

FIGURE 5.5. Shear layer of a dilatant material: drained test. Shear stress and pore pressure at the center versus shear displacement: **(a)** Enhanced finite elements, and **(b)** standard isoparametric formulation.

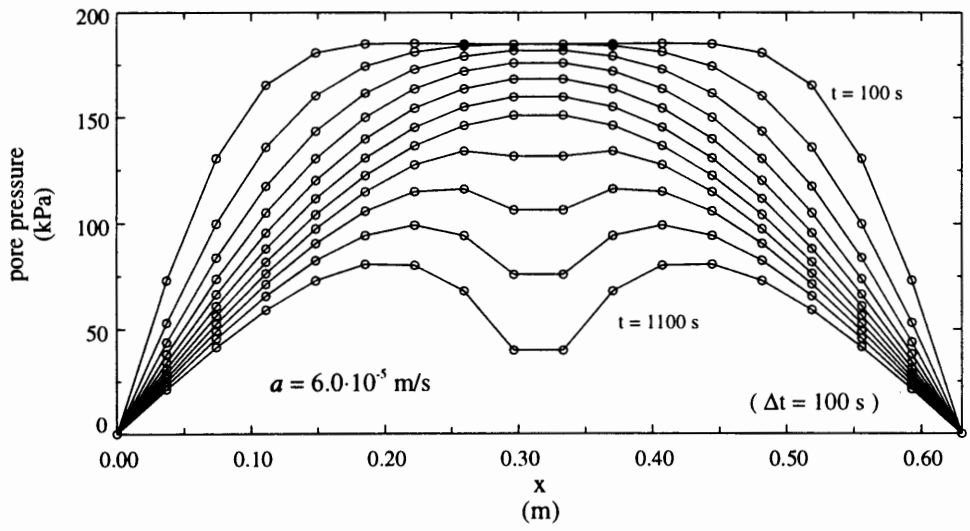

FIGURE 5.6. Shear layer of a dilatant material: drained test. Isochrones of the pore pressure p obtained with the enhanced finite elements for $a = 6 \cdot 10^{-5}\ m/s$ (isochrones shown every 100 s).

strains localize at the center, leading to a sudden increase of the rate of dissipation of the pore pressure, as observed in Figure 5.6 at $t \approx 700\ s$ for the strain rate of $a = 6 \cdot 10^{-5}\ m/s$ and the enhanced finite element formulation This spatial distribution of the pore pressure clearly changes with the formation of the discontinuity, which acts as an internal drainage. Note that negative pressures will eventually appear at the center; the simple model considered in this work does not account for any limitation in this respect, like the cavitation of the fluid.

Comparing the solutions obtained for the two different meshes in Figure 5.5 we can conclude the following. For the proposed enhanced finite element formulation depicted in Figure 5.5.a, a slight difference can be observed between each mesh. The observed differences can be traced back to the different approximation of the fluid flow process by the different spatial discretization and not by a non-objective of the localized dissipative mechanism upon localization. This conclusion is drawn from the same slope obtained in the shear stress plot by both meshes for each imposed strain rate. This situation is to be contrasted with the solutions obtained with the standard isoparametric formulation shown in Figure 5.5.b. The mesh dependence in this case is not only caused by the approximation introduced by the integration of the fluid flow, but clearly also caused by a non-objective resolution of the localized dissipative mechanism. Note the entirely different slopes obtained in the shear stress evolution by the different meshes for each imposed strain rate.

6. Concluding Remarks

We have presented in this paper a general framework for the characterization of strong discontinuities in fully saturated porous media. Discontinuities in the displacements, with the corresponding singular measures of the strains through the associated plastic strains, have been shown to be consistent with a singular distribution of the fluid content. Physically this is a consequence of the dilatant response of these discontinuities, leading to the accumulation of fluid mass along these surfaces of discontinuity and creating a discontinuity of the fluid flow vector across them. The model example of a shear layer of a dilatant material has been used to illustrate these ideas, including the formulation of enhanced strain finite element methods incorporating without regularization these singular fields of the strains and fluid content, as well as the discontinuous fluid flow vectors. The resulting formulation has been shown to avoid the mesh-dependence observed when employing standard isoparametric finite elements based on a local continuum model in the shear driven problems considered herein.

Furthermore, the appearance of these discontinuities has been directly related to the response of the underlying drained material model, as in the discontinuous linearized instabilities observed in the analyses in RICE [1975] and RUDNICKI & RICE [1975], among

others. It is important to emphasize that the fundamental consideration in the developments of the previous sections leading to this result is the continuity of the pressure field (or, more precisely, the regular distributional character of the fluid flow). This consideration is motivated by the structure of the mathematical equations, namely, the involvement of second spatial derivatives of the pressure field in the conservation of fluid mass equation for a *positive permeability*. We also pointed out similar considerations based on experimental observations as reported, for example, in VARDOULAKIS [1996]. As shown in the linearized stability analysis presented in RICE [1975] for a dilatant shear layer, disturbances in the short wave-length limit (zero length scale limit) lead to the instability of the shear layer for the case of a strain softening drained response and physically positive permeability. For the ideal purely undrained case, that is, for zero permeability, the above continuity condition on the pressure is no longer required. As a consequence, the appearance of localization is to be derived from the undrained, rate-independent response of the solid in this ideal limit. The stiffer response of the porous solid under purely undrained conditions puts then a severe demand in the numerical simulations near this limit case, due to the need to capture very accurately the details of the local flow associated to fluid mass conduction. These arguments seem to explain the very sensitive response in the numerical simulations involving a very high strain rate, shown by the difficulty to capture the localized solutions, as indicated in the previous section. Careful analyses of the effects of the spatial and temporal discretizations in the development of these coupled phenomena, including the interaction of the length scales associated to the numerical discretization, the dissipative conduction processes, the assumed imperfections, and strain localization itself, are required. We plan to address these issues in a forthcoming publication.

Similarly, we are currently extending the finite element formulations presented herein to the multi-dimensional case. General states of stress need to be considered, as well as the interaction of possible different length scales in particular states of stress, like the uniaxial compressive examples presented recently in ZHANG & AL [1998]. As shown in ARMERO [1997a], strong discontinuities furnish a very efficient tool for the modeling of localized effects while treating the involved small length scales as unresolvable. The general framework presented in this paper will show to be crucial for this purpose, as it is the current focus of our work in this area.

Acknowledgments: Financial support for this research has been provided by the ONR under contract no. N00014-96-1-0818 and the NSF under contract no. CMS-9703000 with UC Berkeley. C. Callari was supported by a NATO-CNR (Italian National Research Council) scholarship (b. no. 215.29, sett. 11). This support is gratefully acknowledged.

References

ARMERO, F. [1997a] "Large-Scale Modeling of Localized Dissipative Mechanisms in a Local Continuum: Applications to the Numerical Simulation of Strain Localization in Rate-Dependent Inelastic Solids," SEMM/UCB Report no. 97/12, to appear in *Mech. Cohesive-Frictional Mat.*, in press.

ARMERO, F. [1997b] "On the Characterization of Localized Solutions in Inelastic Solids: an Analysis of Wave Propagation in a Softening Bar," SEMM/UCB Report no. 97/18, submitted to *Comp. Meth. Appl. Mech. Eng.*

ARMERO, F. [1998] "Formulation and Finite Element Implementation of a Multiplicative Model of Por-Plasticity at Finite Strains under Fully Saturated Conditions," SEMM/UCB Report no. 98/05, to appear in *Comp. Meth. Appl. Mech. Eng.*, in press.

ARMERO, F. & GARIKIPATI, K. [1995] "Recent Advances in the Analysis and Numerical Simulation of Strain Localization in Inelastic Solids," *Proc. COMPLAS IV,* eds. D.R.J. Owen, E. Onate, and E. Hinton, CIMNE, Barcelona.

ARMERO, F. & GARIKIPATI, K. [1996] "An Analysis of Strong Discontinuities in Multiplicative Finite Strain Plasticity and their Relation with the Numerical Simulation of Strain Localization in Solids," *Int. J. Solids and Structures,* **33**, 2863-2885.

BIOT, M.A. [1941] "General Theory of Three-Dimensional Consolidation," *Journal of Applied Physics,* **12**, 155-164.

COUSSY, O. [1995] *Mechanics of Porous Continua,* Wiley, Chichester.

LARSSON, R. & RUNESSON, K. [1996] "Element Embedded Localization Band Based on Regularized Displacement Discontinuity," *J. Eng. Mech.*, **122**, 402-411.

LARSSON, R.; RUNESSON, K. & STURE, S. [1996] "Embedded Localization Band in Undrained Soil Based on Regularized Strong Discontinuity: Theory and FE Analysis," *Int. J. Solids Structures* **33**, 3081-3101.

LORET, B. & PREVOST, J.H. [1993] "Dynamic Strain Localization in Fluid-Saturated Porous Media," *J. Eng. Mechanics,* **117**, 907-922.

OLIVER, J. [1996] "Modelling Strong Discontinuities in Solid Mechanics via Strain Softening Constitutive Equations. Part 1: Fundamentals. Part 2: Numerical Simulation," *Int. J. Num. Meth. Eng.*, **39**, 3575-3623.

PIETRUSZCZAK, S. [1995] "Undrained Response of Granular Soil Involving Localized Deformation," *J. Eng. Mechanics,* **121**, 1292-1297.

RICE, J.R. [1975] "On the Stability of Dilatant Hardening for Saturated Rock Masses," *J. Geophysical Research,* **80**, 1536-1531.

RUDNICKI, K. & RICE, J.R. [1975] "Conditions for the Localization of Deformation in Pressure-Sensitve Dilatant Materials," *J. Mech. Phys. Solids,* **23**, 371-394.

RUNESSON, K.; PERIC, D. & STURE, S. [1996] "Effect of Pore Fluid Compressibility on Localization in Elastic-Plastic Porous Solids under Undrained Conditions," *Int. J. Solids Structures* **33**, 1501-1518.

SCHREFLER, B.A.; MAJORANA, C.E. & SANAVIA, L. [1995] "Shear Band Localization in Saturated Porous Media" *Arch. Mech.* **47**, 577-599.

SIMO, J.C; OLIVER, J. & ARMERO, F. [1993] "An Analysis of Strong Discontinuities Induced by Softening Solutions in Rate Independent Solids," *J. Comput. Mech.,* **12**, 277-296.

STAKGOLD, I. [1979] *Green's Functions and Boundary Value Problems,* Wiley, New York.

STEINMANN, P.; LARSSON, R. & RUNESSON, K. [1997] "On the Localization Properties of Multiplicative Hyperelasto-plastic Continua with Strong Discontinuities," *Int. Jour. Solids Structures,* **34**, 969-990.

TRUESDELL & NOLL [1965] "The Nonlinear Field Theories of Mechanics," *Handbich der Physik Bd. III/3,* ed. by S. Fluegge, Springer Verlag, Berlin.

VARDOULAKIS, I. [1996] "Deformation of Water-Saturated Sand: I. Uniform Undrained Deformation and Shear Banding; II. Effect of Pore Water Flow and Shear Banding," *Géotechnique,* **46**, 441-472.

ZHANG, H.W.; SANAVIA, L. & SCHREFLER, B.A. [1998] "An Internal Length Scale in Dynamic Strain Localization of Multiphase Porous Media," preprint submitted to *Mech. Cohesive-Frictional Materials.*